

Measurement of the $p\bar{p} \rightarrow t\bar{t}$ production cross section at $\sqrt{s} = 1.96$ TeV in the fully hadronic decay channel

V.M. Abazov,³⁶ B. Abbott,⁷⁵ M. Abolins,⁶⁵ B.S. Acharya,²⁹ M. Adams,⁵² T. Adams,⁵⁰ M. Agelou,¹⁸ J.-L. Agram,¹⁹ S.H. Ahn,³¹ M. Ahsan,⁵⁹ G.D. Alexeev,³⁶ G. Alkhazov,⁴⁰ A. Alton,⁶⁴ G. Alverson,⁶³ G.A. Alves,² M. Anastasoae,³⁵ T. Andeen,⁵⁴ S. Anderson,⁴⁶ B. Andrieu,¹⁷ Y. Arnoud,¹⁴ M. Arov,⁵³ A. Askew,⁵⁰ B. Åsman,⁴¹ A.C.S. Assis Jesus,³ O. Atramentov,⁵⁷ C. Autermann,²¹ C. Avila,⁸ F. Badaud,¹³ A. Baden,⁶¹ L. Bagby,⁵³ B. Baldin,⁵¹ P.W. Balm,³⁴ P. Banerjee,²⁹ S. Banerjee,²⁹ E. Barberis,⁶³ P. Bargassa,⁸⁰ P. Baringer,⁵⁸ C. Barnes,⁴⁴ J. Barreto,² J.F. Bartlett,⁵¹ U. Basser,¹⁷ D. Bauer,⁵⁵ A. Bean,⁵⁸ S. Beauceron,¹⁷ M. Begalli,³ M. Begel,⁷¹ A. Bellavance,⁶⁷ S.B. Beri,²⁷ G. Bernardi,¹⁷ R. Bernhard,⁴² L. Berntzon,¹⁵ I. Bertram,⁴³ M. Besançon,¹⁸ R. Beuselinck,⁴⁴ V.A. Bezzubov,³⁹ P.C. Bhat,⁵¹ V. Bhatnagar,²⁷ M. Binder,²⁵ C. Biscarat,⁴³ K.M. Black,⁶² I. Blackler,⁴⁴ G. Blazey,⁵³ F. Blekman,⁴⁴ S. Blessing,⁵⁰ D. Bloch,¹⁹ U. Blumenschein,²³ A. Boehnlein,⁵¹ O. Boeriu,⁵⁶ T.A. Bolton,⁵⁹ F. Borchering,⁵¹ G. Borissov,⁴³ K. Bos,³⁴ T. Bose,⁷⁰ A. Brandt,⁷⁸ R. Brock,⁶⁵ G. Brooijmans,⁷⁰ A. Bross,⁵¹ D. Brown,⁷⁸ N.J. Buchanan,⁵⁰ D. Buchholz,⁵⁴ M. Buehler,⁸¹ V. Buescher,²³ S. Burdin,⁵¹ S. Burke,⁴⁶ T.H. Burnett,⁸² E. Busato,¹⁷ C.P. Buszello,⁴⁴ J.M. Butler,⁶² S. Calvet,¹⁵ J. Cammin,⁷¹ S. Caron,³⁴ W. Carvalho,³ B.C.K. Casey,⁷⁷ N.M. Cason,⁵⁶ H. Castilla-Valdez,³³ S. Chakrabarti,²⁹ D. Chakraborty,⁵³ K.M. Chan,⁷¹ A. Chandra,²⁹ D. Chapin,⁷⁷ F. Charles,⁷² E. Cheu,⁴⁶ D.K. Cho,⁶² S. Choi,³² B. Choudhary,²⁸ T. Christiansen,²⁵ L. Christofek,⁵⁸ D. Claes,⁶⁷ B. Clément,¹⁹ C. Clément,⁴¹ Y. Coadou,⁵ M. Cooke,⁸⁰ W.E. Cooper,⁵¹ D. Coppage,⁵⁸ M. Corcoran,⁸⁰ M.-C. Cousinou,¹⁵ B. Cox,⁴⁵ S. Crépe-Renaudin,¹⁴ D. Cutts,⁷⁷ H. da Motta,² A. Das,⁶² M. Das,⁶⁰ B. Davies,⁴³ G. Davies,⁴⁴ G.A. Davis,⁵⁴ K. De,⁷⁸ P. de Jong,³⁴ S.J. de Jong,³⁵ E. De La Cruz-Burelo,⁶⁴ C. De Oliveira Martins,³ S. Dean,⁴⁵ J.D. Degenhardt,⁶⁴ F. Déliot,¹⁸ M. Demarteau,⁵¹ R. Demina,⁷¹ P. Demine,¹⁸ D. Denisov,⁵¹ S.P. Denisov,³⁹ S. Desai,⁷² H.T. Diehl,⁵¹ M. Diesburg,⁵¹ M. Doidge,⁴³ H. Dong,⁷² S. Doulas,⁶³ L.V. Dudko,³⁸ L. Dufлот,¹⁶ S.R. Dugad,²⁹ A. Duperrin,¹⁵ J. Dyer,⁶⁵ A. Dyshkant,⁵³ M. Eads,⁶⁷ D. Edmunds,⁶⁵ T. Edwards,⁴⁵ J. Ellison,⁴⁹ J. Elmsheuser,²⁵ V.D. Elvira,⁵¹ S. Eno,⁶¹ P. Ermolov,³⁸ J. Estrada,⁵¹ H. Evans,⁵⁵ A. Evdokimov,³⁷ V.N. Evdokimov,³⁹ J. Fast,⁵¹ S.N. Fatakia,⁶² L. Feligioni,⁶² A.V. Ferapontov,³⁹ T. Ferbel,⁷¹ F. Fiedler,²⁵ F. Filthaut,³⁵ W. Fisher,⁵¹ H.E. Fisk,⁵¹ I. Fleck,²³ M. Fortner,⁵³ H. Fox,²³ S. Fu,⁵¹ S. Fuess,⁵¹ T. Gadfort,⁸² C.F. Galea,³⁵ E. Gallas,⁵¹ E. Galyaev,⁵⁶ C. Garcia,⁷¹ A. Garcia-Bellido,⁸² J. Gardner,⁵⁸ V. Gavrilov,³⁷ A. Gay,¹⁹ P. Gay,¹³ D. Gelé,¹⁹ R. Gelhaus,⁴⁹ C.E. Gerber,⁵² Y. Gershtein,⁵⁰ D. Gillberg,⁵ G. Ginther,⁷¹ T. Golling,²² N. Gollub,⁴¹ B. Gómez,⁸ K. Gounder,⁵¹ A. Goussiou,⁵⁶ P.D. Grannis,⁷² S. Greder,³ H. Greenlee,⁵¹ Z.D. Greenwood,⁶⁰ E.M. Gregores,⁴ G. Grenier,²⁰ Ph. Gris,¹³ J.-F. Grivaz,¹⁶ S. Grünendahl,⁵¹ M.W. Grünewald,³⁰ G. Gutierrez,⁵¹ P. Gutierrez,⁷⁵ A. Haas,⁷⁰ N.J. Hadley,⁶¹ S. Hagopian,⁵⁰ J. Haley,⁶⁸ I. Hall,⁷⁵ R.E. Hall,⁴⁸ C. Han,⁶⁴ L. Han,⁷ K. Hanagaki,⁵¹ K. Harder,⁵⁹ A. Harel,²⁶ R. Harrington,⁶³ J.M. Hauptman,⁵⁷ R. Hauser,⁶⁵ J. Hays,⁵⁴ T. Hebbeker,²¹ D. Hedin,⁵³ J.G. Hegeman,³⁴ J.M. Heinmiller,⁵² A.P. Heinson,⁴⁹ U. Heintz,⁶² C. Hensel,⁵⁸ G. Hesketh,⁶³ M.D. Hildreth,⁵⁶ R. Hirosky,⁸¹ J.D. Hobbs,⁷² B. Hoeneisen,¹² M. Hohlfield,¹⁶ S.J. Hong,³¹ R. Hooper,⁷⁷ P. Houben,³⁴ Y. Hu,⁷² J. Huang,⁵⁵ V. Hynek,⁹ I. Iashvili,⁶⁹ R. Illingworth,⁵¹ A.S. Ito,⁵¹ S. Jabeen,⁵⁸ M. Jaffré,¹⁶ S. Jain,⁷⁵ V. Jain,⁷³ K. Jakobs,²³ C. Jarvis,⁶¹ A. Jenkins,⁴⁴ R. Jesik,⁴⁴ K. Johns,⁴⁶ C. Johnson,⁷⁰ M. Johnson,⁵¹ A. Jonckheere,⁵¹ P. Jonsson,⁴⁴ A. Juste,⁵¹ D. Käfer,²¹ S. Kahn,⁷³ E. Kajfasz,¹⁵ A.M. Kalinin,³⁶ J.M. Kalk,⁶⁰ J.R. Kalk,⁶⁵ D. Karmanov,³⁸ J. Kasper,⁶² I. Katsanos,⁷⁰ D. Kau,⁵⁰ R. Kaur,²⁷ R. Kehoe,⁷⁹ S. Kermiche,¹⁵ S. Kesiosoglou,⁷⁷ A. Khanov,⁷⁶ A. Kharchilava,⁶⁹ Y.M. Kharzheev,³⁶ D. Khatidze,⁷⁰ H. Kim,⁷⁸ T.J. Kim,³¹ B. Klima,⁵¹ J.M. Kohli,²⁷ J.-P. Konrath,²³ M. Kopal,⁷⁵ V.M. Korablev,³⁹ J. Kotcher,⁷³ B. Kothari,⁷⁰ A. Koubarovsky,³⁸ A.V. Kozelov,³⁹ J. Kozminski,⁶⁵ A. Kryemadhi,⁸¹ S. Krzywdzinski,⁵¹ A. Kumar,⁶⁹ S. Kunori,⁶¹ A. Kupco,¹¹ T. Kurča,²⁰ J. Kvita,⁹ S. Lager,⁴¹ S. Lammers,⁷⁰ G. Landsberg,⁷⁷ J. Lazoflores,⁵⁰ A.-C. Le Bihan,¹⁹ P. Lebrun,²⁰ W.M. Lee,⁵⁰ A. Leflat,³⁸ F. Lehner,⁴² C. Leonidopoulos,⁷⁰ V. Lesne,¹³ J. Leveque,⁴⁶ P. Lewis,⁴⁴ J. Li,⁷⁸ Q.Z. Li,⁵¹ J.G.R. Lima,⁵³ D. Lincoln,⁵¹ S.L. Linn,⁵⁰ J. Linnemann,⁶⁵ V.V. Lipaev,³⁹ R. Lipton,⁵¹ L. Lobo,⁴⁴ A. Lobodenko,⁴⁰ M. Lokajicek,¹¹ A. Lounis,¹⁹ P. Love,⁴³ H.J. Lubatti,⁸² L. Lueking,⁵¹ M. Lynker,⁵⁶ A.L. Lyon,⁵¹ A.K.A. Maciel,² R.J. Madaras,⁴⁷ P. Mättig,²⁶ C. Magass,²¹ A. Magerkurth,⁶⁴ A.-M. Magnan,¹⁴ N. Makovec,¹⁶ P.K. Mal,⁵⁶ H.B. Malbouisson,³ S. Malik,⁶⁷ V.L. Malyshev,³⁶ H.S. Mao,⁶ Y. Maravin,⁵⁹ M. Martens,⁵¹ S.E.K. Mattingly,⁷⁷ R. McCarthy,⁷² R. McCroskey,⁴⁶ D. Meder,²⁴ A. Melnitchouk,⁶⁶ A. Mendes,¹⁵ L. Mendoza,⁸ M. Merkin,³⁸ K.W. Merritt,⁵¹ A. Meyer,²¹ J. Meyer,²² M. Michaut,¹⁸ H. Miettinen,⁸⁰ J. Mitrevski,⁷⁰ J. Molina,³ N.K. Mondal,²⁹ J. Monk,⁴⁵ R.W. Moore,⁵ T. Moulik,⁵⁸ G.S. Muanza,²⁰ M. Mulders,⁵¹ L. Mundim,³ Y.D. Mutaf,⁷² E. Nagy,¹⁵ M. Naimuddin,²⁸ M. Narain,⁶² N.A. Naumann,³⁵ H.A. Neal,⁶⁴ J.P. Negret,⁸

S. Nelson,⁵⁰ P. Neustroev,⁴⁰ C. Noeding,²³ A. Nomerotski,⁵¹ S.F. Novaes,⁴ T. Nunnemann,²⁵ E. Nurse,⁴⁵ V. O'Dell,⁵¹ D.C. O'Neil,⁵ G. Odrant,⁴⁰ V. Oguri,³ N. Oliveira,³ N. Oshima,⁵¹ G.J. Otero y Garzón,⁵² P. Padley,⁸⁰ N. Parashar,^{51,*} S.K. Park,³¹ J. Parsons,⁷⁰ R. Partridge,⁷⁷ N. Parua,⁷² A. Patwa,⁷³ G. Pawloski,⁸⁰ P.M. Perea,⁴⁹ E. Perez,¹⁸ P. Pétroff,¹⁶ M. Petteni,⁴⁴ R. Piegai,¹ M.-A. Pleier,²² P.L.M. Podesta-Lerma,³³ V.M. Podstavkov,⁵¹ Y. Pogorelov,⁵⁶ M.-E. Pol,² A. Pompoš,⁷⁵ B.G. Pope,⁶⁵ W.L. Prado da Silva,³ H.B. Prosper,⁵⁰ S. Protopopescu,⁷³ J. Qian,⁶⁴ A. Quadt,²² B. Quinn,⁶⁶ K.J. Rani,²⁹ K. Ranjan,²⁸ P.A. Rapidis,⁵¹ P.N. Ratoff,⁴³ S. Reucroft,⁶³ M. Rijssenbeek,⁷² I. Ripp-Baudot,¹⁹ F. Rizatdinova,⁷⁶ S. Robinson,⁴⁴ R.F. Rodrigues,³ C. Royon,¹⁸ P. Rubinov,⁵¹ R. Ruchti,⁵⁶ V.I. Rud,³⁸ G. Sajot,¹⁴ A. Sánchez-Hernández,³³ M.P. Sanders,⁶¹ A. Santoro,³ G. Savage,⁵¹ L. Sawyer,⁶⁰ T. Scanlon,⁴⁴ D. Schaile,²⁵ R.D. Schamberger,⁷² Y. Scheglov,⁴⁰ H. Schellman,⁵⁴ P. Schieferdecker,²⁵ C. Schmitt,²⁶ C. Schwanenberger,²² A. Schwartzman,⁶⁸ R. Schwienhorst,⁶⁵ S. Sengupta,⁵⁰ H. Severini,⁷⁵ E. Shabalina,⁵² M. Shamim,⁵⁹ V. Shary,¹⁸ A.A. Shchukin,³⁹ W.D. Shephard,⁵⁶ R.K. Shivpuri,²⁸ D. Shpakov,⁶³ R.A. Sidwell,⁵⁹ V. Simak,¹⁰ V. Sirotenko,⁵¹ P. Skubic,⁷⁵ P. Slattery,⁷¹ R.P. Smith,⁵¹ K. Smolek,¹⁰ G.R. Snow,⁶⁷ J. Snow,⁷⁴ S. Snyder,⁷³ S. Söldner-Rembold,⁴⁵ X. Song,⁵³ L. Sonnenschein,¹⁷ A. Sopczak,⁴³ M. Sosebee,⁷⁸ K. Soustruznik,⁹ M. Souza,² B. Spurlock,⁷⁸ J. Stark,¹⁴ J. Steele,⁶⁰ K. Stevenson,⁵⁵ V. Stolin,³⁷ A. Stone,⁵² D.A. Stoyanova,³⁹ J. Strandberg,⁴¹ M.A. Strang,⁶⁹ M. Strauss,⁷⁵ R. Ströhmer,²⁵ D. Strom,⁵⁴ M. Strovink,⁴⁷ L. Stutte,⁵¹ S. Sumowidagdo,⁵⁰ A. Sznajder,³ M. Talby,¹⁵ P. Tamburello,⁴⁶ W. Taylor,⁵ P. Telford,⁴⁵ J. Temple,⁴⁶ B. Tiller,²⁵ M. Titov,²³ M. Tomoto,⁵¹ T. Toole,⁶¹ I. Torchiani,²³ S. Towers,⁴³ T. Trefzger,²⁴ S. Trincas-Duvoid,¹⁷ D. Tsybychev,⁷² B. Tuchming,¹⁸ C. Tully,⁶⁸ A.S. Turcot,⁴⁵ P.M. Tuts,⁷⁰ L. Uvarov,⁴⁰ S. Uvarov,⁴⁰ S. Uzunyan,⁵³ B. Vachon,⁵ P.J. van den Berg,³⁴ R. Van Kooten,⁵⁵ W.M. van Leeuwen,³⁴ N. Varelas,⁵² E.W. Varnes,⁴⁶ A. Vartapetian,⁷⁸ I.A. Vasilyev,³⁹ M. Vaupel,²⁶ P. Verdier,²⁰ L.S. Vertogradov,³⁶ M. Verzocchi,⁵¹ F. Villeneuve-Seguiet,⁴⁴ J.-R. Vlimant,¹⁷ E. Von Toerne,⁵⁹ M. Voutilainen,^{67,†} M. Vreeswijk,³⁴ T. Vu Anh,¹⁶ H.D. Wahl,⁵⁰ L. Wang,⁶¹ J. Warchol,⁵⁶ G. Watts,⁸² M. Wayne,⁵⁶ M. Weber,⁵¹ H. Weerts,⁶⁵ N. Worms,²² M. Wetstein,⁶¹ A. White,⁷⁸ V. White,⁵¹ D. Wicke,⁵¹ D.A. Wijngaarden,³⁵ G.W. Wilson,⁵⁸ S.J. Wimpenny,⁴⁹ M. Wobisch,⁵¹ J. Womersley,⁵¹ D.R. Wood,⁶³ T.R. Wyatt,⁴⁵ Y. Xie,⁷⁷ Q. Xu,⁶⁴ N. Xuan,⁵⁶ S. Yacoub,⁵⁴ R. Yamada,⁵¹ M. Yan,⁶¹ T. Yasuda,⁵¹ Y.A. Yatsunenko,³⁶ Y. Yen,²⁶ K. Yip,⁷³ H.D. Yoo,⁷⁷ S.W. Youn,⁵⁴ J. Yu,⁷⁸ A. Yurkewicz,⁷² A. Zabi,¹⁶ A. Zatserklyaniy,⁵³ C. Zeitnitz,²⁴ D. Zhang,⁵¹ T. Zhao,⁸² Z. Zhao,⁶⁴ B. Zhou,⁶⁴ J. Zhu,⁷² M. Zielinski,⁷¹ D. Zieminska,⁵⁵ A. Zieminski,⁵⁵ V. Zutshi,⁵³ and E.G. Zverev³⁸

(DØ Collaboration)

¹Universidad de Buenos Aires, Buenos Aires, Argentina

²LAFEX, Centro Brasileiro de Pesquisas Físicas, Rio de Janeiro, Brazil

³Universidade do Estado do Rio de Janeiro, Rio de Janeiro, Brazil

⁴Instituto de Física Teórica, Universidade Estadual Paulista, São Paulo, Brazil

⁵University of Alberta, Edmonton, Alberta, Canada, Simon Fraser University, Burnaby, British Columbia, Canada, York University, Toronto, Ontario, Canada, and McGill University, Montreal, Quebec, Canada

⁶Institute of High Energy Physics, Beijing, People's Republic of China

⁷University of Science and Technology of China, Hefei, People's Republic of China

⁸Universidad de los Andes, Bogotá, Colombia

⁹Center for Particle Physics, Charles University, Prague, Czech Republic

¹⁰Czech Technical University, Prague, Czech Republic

¹¹Center for Particle Physics, Institute of Physics, Academy of Sciences of the Czech Republic, Prague, Czech Republic

¹²Universidad San Francisco de Quito, Quito, Ecuador

¹³Laboratoire de Physique Corpusculaire, IN2P3-CNRS, Université Blaise Pascal, Clermont-Ferrand, France

¹⁴Laboratoire de Physique Subatomique et de Cosmologie, IN2P3-CNRS, Université de Grenoble 1, Grenoble, France

¹⁵CPPM, IN2P3-CNRS, Université de la Méditerranée, Marseille, France

¹⁶IN2P3-CNRS, Laboratoire de l'Accélérateur Linéaire, Orsay, France

¹⁷LPNHE, IN2P3-CNRS, Universités Paris VI and VII, Paris, France

¹⁸DAPNIA/Service de Physique des Particules, CEA, Saclay, France

¹⁹IReS, IN2P3-CNRS, Université Louis Pasteur, Strasbourg, France, and Université de Haute Alsace, Mulhouse, France

²⁰Institut de Physique Nucléaire de Lyon, IN2P3-CNRS, Université Claude Bernard, Villeurbanne, France

²¹III. Physikalisches Institut A, RWTH Aachen, Aachen, Germany

²²Physikalisches Institut, Universität Bonn, Bonn, Germany

²³Physikalisches Institut, Universität Freiburg, Freiburg, Germany

²⁴Institut für Physik, Universität Mainz, Mainz, Germany

²⁵Ludwig-Maximilians-Universität München, München, Germany

²⁶Fachbereich Physik, University of Wuppertal, Wuppertal, Germany

²⁷Panjab University, Chandigarh, India

²⁸Delhi University, Delhi, India

²⁹Tata Institute of Fundamental Research, Mumbai, India

³⁰University College Dublin, Dublin, Ireland

- ³¹ Korea Detector Laboratory, Korea University, Seoul, Korea
³² SungKyunKwan University, Suwon, Korea
³³ CINVESTAV, Mexico City, Mexico
³⁴ FOM-Institute NIKHEF and University of Amsterdam/NIKHEF, Amsterdam, The Netherlands
³⁵ Radboud University Nijmegen/NIKHEF, Nijmegen, The Netherlands
³⁶ Joint Institute for Nuclear Research, Dubna, Russia
³⁷ Institute for Theoretical and Experimental Physics, Moscow, Russia
³⁸ Moscow State University, Moscow, Russia
³⁹ Institute for High Energy Physics, Protvino, Russia
⁴⁰ Petersburg Nuclear Physics Institute, St. Petersburg, Russia
⁴¹ Lund University, Lund, Sweden, Royal Institute of Technology and Stockholm University, Stockholm, Sweden, and Uppsala University, Uppsala, Sweden
⁴² Physik Institut der Universität Zürich, Zürich, Switzerland
⁴³ Lancaster University, Lancaster, United Kingdom
⁴⁴ Imperial College, London, United Kingdom
⁴⁵ University of Manchester, Manchester, United Kingdom
⁴⁶ University of Arizona, Tucson, Arizona 85721, USA
⁴⁷ Lawrence Berkeley National Laboratory and University of California, Berkeley, California 94720, USA
⁴⁸ California State University, Fresno, California 93740, USA
⁴⁹ University of California, Riverside, California 92521, USA
⁵⁰ Florida State University, Tallahassee, Florida 32306, USA
⁵¹ Fermi National Accelerator Laboratory, Batavia, Illinois 60510, USA
⁵² University of Illinois at Chicago, Chicago, Illinois 60607, USA
⁵³ Northern Illinois University, DeKalb, Illinois 60115, USA
⁵⁴ Northwestern University, Evanston, Illinois 60208, USA
⁵⁵ Indiana University, Bloomington, Indiana 47405, USA
⁵⁶ University of Notre Dame, Notre Dame, Indiana 46556, USA
⁵⁷ Iowa State University, Ames, Iowa 50011, USA
⁵⁸ University of Kansas, Lawrence, Kansas 66045, USA
⁵⁹ Kansas State University, Manhattan, Kansas 66506, USA
⁶⁰ Louisiana Tech University, Ruston, Louisiana 71272, USA
⁶¹ University of Maryland, College Park, Maryland 20742, USA
⁶² Boston University, Boston, Massachusetts 02215, USA
⁶³ Northeastern University, Boston, Massachusetts 02115, USA
⁶⁴ University of Michigan, Ann Arbor, Michigan 48109, USA
⁶⁵ Michigan State University, East Lansing, Michigan 48824, USA
⁶⁶ University of Mississippi, University, Mississippi 38677, USA
⁶⁷ University of Nebraska, Lincoln, Nebraska 68588, USA
⁶⁸ Princeton University, Princeton, New Jersey 08544, USA
⁶⁹ State University of New York, Buffalo, New York 14260, USA
⁷⁰ Columbia University, New York, New York 10027, USA
⁷¹ University of Rochester, Rochester, New York 14627, USA
⁷² State University of New York, Stony Brook, New York 11794, USA
⁷³ Brookhaven National Laboratory, Upton, New York 11973, USA
⁷⁴ Langston University, Langston, Oklahoma 73050, USA
⁷⁵ University of Oklahoma, Norman, Oklahoma 73019, USA
⁷⁶ Oklahoma State University, Stillwater, Oklahoma 74078, USA
⁷⁷ Brown University, Providence, Rhode Island 02912, USA
⁷⁸ University of Texas, Arlington, Texas 76019, USA
⁷⁹ Southern Methodist University, Dallas, Texas 75275, USA
⁸⁰ Rice University, Houston, Texas 77005, USA
⁸¹ University of Virginia, Charlottesville, Virginia 22901, USA
⁸² University of Washington, Seattle, Washington 98195, USA

(Dated: May 31, 2006)

A measurement of the top quark pair production cross section in proton anti-proton collisions at an interaction energy of $\sqrt{s} = 1.96$ TeV is presented. This analysis uses 350 pb^{-1} of data collected with the DØ detector at the Fermilab Tevatron Collider. The data sample consists of multijet events with six or more reconstructed jets, consistent with fully hadronic $t\bar{t}$ decay. An analysis combining secondary vertex tagging and a neural network yields a cross section of $\sigma_{t\bar{t}} = 5.2_{-2.2}^{+2.3}(\text{stat})_{-1.2}^{+1.6}(\text{syst}) \pm 0.3(\text{lumi}) \text{ pb}$.

PACS numbers:

The standard model (SM) predicts that top quarks decay primarily into a W boson and a b quark. The measurement presented in this letter tests the prediction of the SM in the dominant decay mode of the $t\bar{t}$ system: when both W bosons decay to quarks, the so-called fully hadronic decay channel. This topology occurs in 46% of $t\bar{t}$ events. The signature for fully hadronic $t\bar{t}$ events is six reconstructed jets, originating from the hadronization of the six quarks. Of the six jets, two originate from b quark decay. Fully hadronic $t\bar{t}$ events are difficult to identify at the Fermilab Tevatron Collider, because the background rate is many orders of magnitude larger than that of the $t\bar{t}$ signal[1].

In this letter, we report a measurement of the production cross-section $\sigma_{t\bar{t}}$ of top quark pairs, using data collected with DØ in the fully hadronic channel, that exploits the long lifetime of the b -hadrons to identify b -jets. To increase our sensitivity for $t\bar{t}$ events, we use a neural network to distinguish signal from the overwhelming background of light-quark QCD multijet production.

The DØ detector has a central tracking system, consisting of a silicon micro strip tracker (SMT) and a central fiber tracker (CFT), both located within a 2 T superconducting solenoidal magnet [2], with designs optimised for tracking and vertexing at pseudorapidities $|\eta| < 3$ and $|\eta| < 2.5$ [14], respectively. The liquid-argon and uranium calorimeter has a central section (CC) covering pseudorapidities $|\eta|$ up to ≈ 1.1 and two end calorimeters (EC) that extend coverage to $|\eta| \approx 4.2$, with all three housed in separate cryostats. An outer muon system, at $|\eta| < 2$, consists of a layer of tracking detectors and scintillation trigger counters in front of 1.8 T toroids, followed by two similar layers after the toroids. Luminosity is measured using plastic scintillator arrays placed in front of the EC cryostats [3]. The trigger and data acquisition systems are designed to accommodate the high luminosities of the Fermilab Tevatron Collider.

The dataset was collected between 2002 and 2004, and corresponds to an integrated luminosity $\mathcal{L} = 350 \pm 23 \text{ pb}^{-1}$. To isolate events with six jets, we use a dedicated multijet trigger that requires three or four trigger towers at the lowest trigger level, three reconstructed simple cone jets at the second trigger level [2], combined with a requirement on the sum of the transverse momenta of the jets, and four or five reconstructed cone jets at the highest trigger level. The trigger was tuned for the fully hadronic $t\bar{t}$ channel and is optimised to remain as efficient as possible while still only using limited bandwidth. The collection rate after all trigger levels was fixed to a few Hz, which is completely dominated by QCD multijet events. The requirements on the jet energy threshold were tightened during the collection of the dataset, to manage the increasing instantaneous luminosities delivered by the Fermilab Tevatron Collider during the period.

We simulated $t\bar{t}$ production using ALPGEN [10] to generate the parton-level processes, and PYTHIA [11] to model hadronisation. The decay of hadrons carrying bot-

tom quarks was modeled using EVTGEN [12]. The simulated $t\bar{t}$ events were processed with the full GEANT-based [9] DØ detector simulation, after which the Monte Carlo (MC) events are passed through the same reconstruction program as was used for data. The small differences between the MC model and the data were corrected for by additional smearing of the reconstructed objects. The residual differences were very small and were corrected for using factors derived from detailed comparisons between the MC model and the data for well understood SM processes such as Z boson and QCD dijet production.

In the off-line analysis, jets were defined with an iterative cone algorithm [4]. Before the jet algorithm was applied, calorimeter noise was suppressed by removing isolated cells whose measured energy is lower than four standard deviations above cell pedestal. In the event that a cell was adjacent to such a cell, it was retained if its signal exceeded 2.5 standard deviations above pedestal. Cells with negative energies were always removed. The elements for cone jet reconstruction consisted of projective towers of calorimeter cells. First, a simple cone algorithm was run on the calorimeter towers. This continued until all towers with energies over 500 MeV had been associated with a simple cone jet. The simple cone jets (proto-jets) are the seeds for the iterative cone algorithm which was run over all calorimeter towers. In addition a midpoint clustering was applied, where any combination of two proto-jets was used as a seed for a possible additional proto-jet, but only if the two proto-jets were within one and two cone distances of each other. The midpoint clustering was added to decrease the sensitivity to soft radiation.

At this stage, the jet candidates that share energy were examined with a splitting and merging algorithm, after which each calorimeter tower belonged to one jet at most. The jets were merged if the shared p_T exceeds 50% of the p_T of the larger jet and the cells were added to the most energetic proto-jet while the other candidate was rejected. If the proto-jets shared less than half of their energy, the shared cells were assigned to the proto-jet which was closest in ΔR space, where $\Delta R = \sqrt{(\Delta y)^2 + (\Delta \phi)^2}$, y is the rapidity and ϕ the azimuthal angle. The final jet reconstruction is an iterative process to form stable cones around the proto-jets. This process was iterated until a stable collection of jets is found, which are then referred to as the *reconstructed* jets in the event. As the jets from $t\bar{t}$ production are relatively narrow due to their transverse momenta, the jets were defined using a cone with radius $\Delta R = 0.5$. The minimal transverse momentum of a reconstructed jet is 8 GeV/c before any energy corrections are applied, a limit dictated by the resolution of the calorimeter.

To remove isolated electromagnetic particles, the fraction of their energy in the electromagnetic calorimeter (EMF) was required to be less than 0.95. Jets with more than 0.4 of their energy in the coarse hadronic calorimeter were rejected, as were jets with $EMF < 0.05$ to ensure no jets were used that were purely hadronic. Jets clus-

tered from hot cell clusters or single hot towers are also rejected. The remaining noise contribution is removed by requiring that the jet also fired the first level trigger, which is insensitive to electronics noise.

To correct the calorimeter jet energies back to the particle level, a jet energy scale (JES) correction C^{JES} was applied [15]. As the calorimeter behavior is not necessarily correctly modeled in Monte Carlo simulation, it is also necessary to correct simulated jets. The value of the energy correction depends on the cone size used in the jet reconstruction. The particle level or true jet energy E^{true} is obtained from the measured jet energy E^m using the relation

$$E^{true} = \frac{E^m - E_0(y, \mathcal{L})}{\mathcal{R}(y, E^m)S(y, E^m)} = C^{JES}(E^m, y, \mathcal{L}) \cdot E^m. \quad (1)$$

The total correction is applied to the measured energy E^m as a multiplicative factor C^{JES} .

The inputs for C^{JES} are E_0 , \mathcal{R} and S . $E_0(y, \mathcal{L})$ is the offset created by detector and electronic noise, pile-up energy from previous collisions and the additional energy from the underlying physics event. The dependence on the luminosity \mathcal{L} is caused by the fact that the number of additional interactions is dependent on the instantaneous luminosity, while the dependence on y is caused by changes in the calorimeter occupancy as a function of the jet rapidity. $\mathcal{R}(y, E^m)$ parameterises the energy response of the calorimeter, while $S(y, E^m)$ represents the fraction of the jet that is deposited inside the jet cone. This out-of-cone showering correction depends not only on the cone size of the jet but also on the energy of the jet and location in the calorimeter.

The JES is measured directly using p_T conservation in photon + jet events. The method is identical for data and simulation. In the simplest case, the jet balances the photon in the transverse plane. As the energy of the photon can be directly and accurately measured (the electromagnetic calorimeter response is accurately known from measurements of resonances in the e^+e^- spectrum like J/ψ and the Z boson and photonic π^0 decays), the true jet energy can be derived from the difference between the photon and jet energy. The response of the E_0 , \mathcal{R} and S are fit as a function of jet rapidity and measured energy, which leads to uncertainties coming from the fit (statistical) and the method (systematic). The total correction C^{JES} is around 1.4 for data. The uncertainties on C^{JES} , which are dominated by the systematic correction for the out-of-cone showering $S(y, E^m)$, are of the order of a few percent, and are very dependent of the jet energy and rapidity.

The jet energy resolution was measured in photon + jet data for low jet energies and dijet data for higher jet energy values. Fits to the transverse energy asymmetry $[p_T(1) - p_T(2)]/[p_T(1) + p_T(2)]$ are then used to obtain the jet energy resolution, which is measured as a function of jet rapidity and transverse energy. The uncertainties on the jet energy resolution are dominated by the fit uncertainty and limited statistics in the samples used.

TABLE I: Efficiency for selection criteria applied before b -jet identification. We choose to define the trigger efficiency for events with six or more jets only and it is determined after preselection. The errors are due to Monte Carlo statistics.

cut	$t\bar{t} \rightarrow \text{hadrons}$	$t\bar{t} \rightarrow \ell + \text{jets}$	any $t\bar{t}$
preselection	0.2706 ± 0.0016	0.0311 ± 0.0008	0.1385 ± 0.0011
trigger	0.2527 ± 0.0015	0.0268 ± 0.0007	0.1284 ± 0.0010

We used events with four or more reconstructed jets, in which the scalar sum of the uncorrected transverse momenta H_T of all the jets in the event was greater than 90 GeV/c. We required at least six jets with corrected transverse momentum > 15 GeV/c. Events with isolated leptons were vetoed to ensure that the all-hadronic and leptonic samples were disjoint [5]. In addition, we rejected events that include two distinct multijet events with separate primary vertices. The primary vertex requirement does not affect minimum bias interactions or $t\bar{t}$ events. The efficiency for the preselection and trigger is listed in Table I, which lists the efficiency for the fully hadronic decay channel. A small contribution from the semi-leptonic (lepton+jets) $t\bar{t}$ channels is also expected. The combined efficiency includes the fully hadronic and semi-leptonic W^+W^- branching fractions of 0.4619 ± 0.0048 and 0.4349 ± 0.0027 respectively [8].

We used a secondary vertex tagging algorithm (SVT) to identify b -quark jets. The algorithm is the same as used in previously published $D\bar{O} t\bar{t}$ production cross section measurements [5]. Secondary vertex candidates were reconstructed from two or more tracks in the jet and candidate long-lived non- b hadrons like K_S^0 and Λ were rejected. Two working points are used; these are labeled “loose” and “tight” respectively. If a reconstructed secondary vertex in the jet had a transverse decay length L_{xy} significance $(L_{xy}/\sigma_{L_{xy}}) > 5(7)$, the jet was tagged as a loose (tight) b -quark jet. Events with two or more loosely tagged jets were referred to as double-tag events. The remaining sample is searched for events with one tight tag. Events thus isolated are labeled single-tag events. Single-tag and double-tag events were treated separately because of their different signal-to-background ratios. The tight SVT is optimized for the rejection of mistags, the main background in the single-tag analysis. When two tags are required, the background sample starts to be dominated by $b\bar{b}$. The choice to use the loose SVT optimizes the double-tag analysis for signal efficiency instead of background rejection.

Compared to light-quark QCD multijet events, $t\bar{t}$ events on average have more jets, of higher energy, with less boost in the beam direction, resulting in events with many, centrally located jets of similar energy. Moreover, the fully hadronic decay makes it possible, in principle, to reconstruct the W boson and t quark four-vectors. To distinguish between signal and background, we used the following event characteristics [6]:

(1) H_T : The scalar sum of the transverse momenta of the jets. Figure 1 shows the H_T distribution for single-

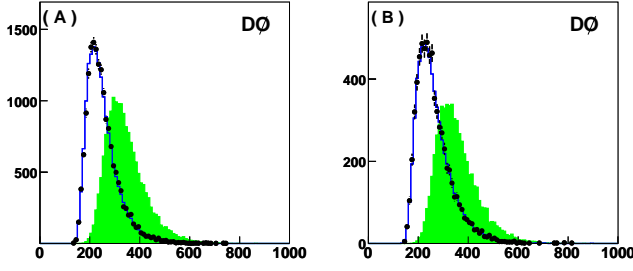


FIG. 1: The H_T distribution for single-tag events (A) and double-tag events (B). Shown are the data (points), the background (solid line) and the expected $t\bar{t}$ distribution (filled histogram) multiplied by 140(60) for the single(double)-tag analysis.

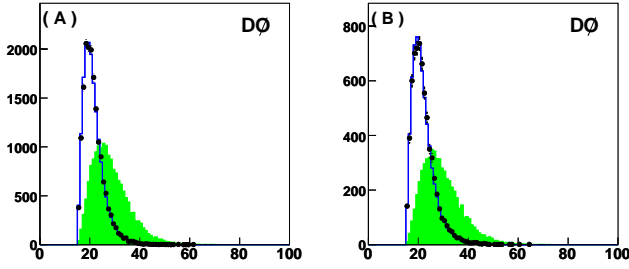


FIG. 2: The E_T^{56} distribution for single-tag events (A) and double-tag events (B). Shown are the data (points), the background (solid line) and the expected $t\bar{t}$ distribution (filled histogram) multiplied by 140(60) for the single(double)-tag analysis.

and double-tag events.

(2) E_T^{56} : The square root of the product of the transverse momenta of the fifth and sixth jet. Figure 2 shows the E_T^{56} distribution for single- and double-tag events.

(3) \mathcal{A} : The aplanarity as calculated from the normalised momentum tensor. Figure 3 shows the \mathcal{A} distribution for single- and double-tag events.

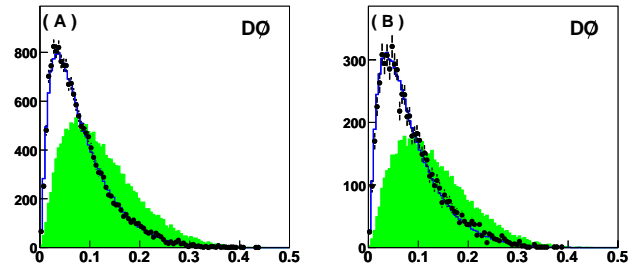


FIG. 3: The \mathcal{A} distribution for single-tag events (A) and double-tag events (B). Shown are the data (points), the background (solid line) and the expected $t\bar{t}$ distribution (filled histogram) multiplied by 140(60) for the single(double)-tag analysis.

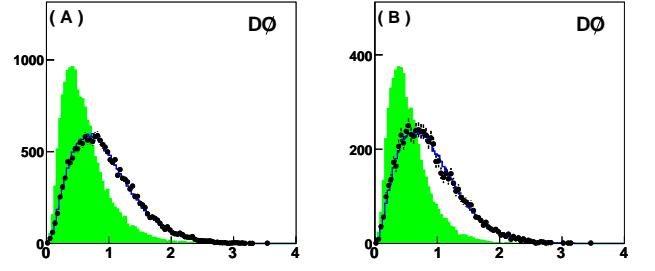


FIG. 4: The $\langle\eta^2\rangle$ distribution for single-tag events (A) and double-tag events (B). Shown are the data (points), the background (solid line) and the expected $t\bar{t}$ distribution (filled histogram) multiplied by 140(60) for the single(double)-tag analysis.

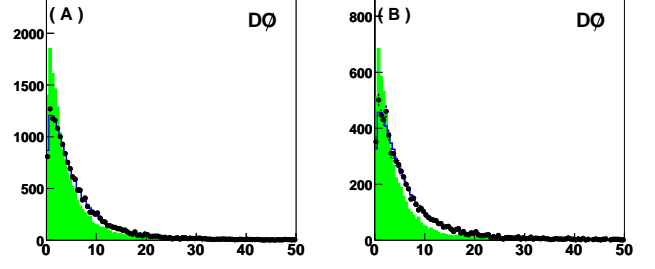


FIG. 5: The \mathcal{M} distribution for single-tag events (A) and double-tag events (B). Shown are the data (points), the background (solid line) and the expected $t\bar{t}$ distribution (filled histogram) multiplied by 140(60) for the single(double)-tag analysis.

tribution for single- and double-tag events.

(4) $\langle\eta^2\rangle$: The p_T -weighted mean square of the η distribution of the jets in an event. Figure 4 shows the $\langle\eta^2\rangle$ distribution for single- and double-tag events.

(5) \mathcal{M} : The mass- χ^2 variable, which is defined as $\mathcal{M} = (M_{W_1} - M_W)^2/\sigma_{M_W}^2 + (M_{W_2} - M_W)^2/\sigma_{M_W}^2 + (m_{t_1} - m_{t_2})^2/\sigma_{m_t}^2$, where the parameters M_W , σ_{M_W} and σ_{m_t} are set to the values obtained from MC, respectively 79, 11 and 21 GeV/c². M_{W_i} and m_{t_i} are obtained from the combination of jets that yields the lowest value of \mathcal{M} , where we do not distinguish between tagged and untagged jets. Figure 5 shows the \mathcal{M} distribution for single- and double-tag events.

(6) M_{min}^{34} : The second-smallest dijet mass in the event. First, all possible dijet masses are considered and the jets that yield the smallest mass are rejected. M_{min}^{34} is the smallest dijet mass as found from the remaining jets. Figure 6 shows the M_{min}^{34} distribution for single- and double-tag events.

The top quark production cross section is calculated from the output of NN_{all} , an artificial neural network trained to force its output near 1 for $t\bar{t}$ events and near -1 for QCD events, using the multilayer perceptron in the ROOT analysis program [7]. The very large background-

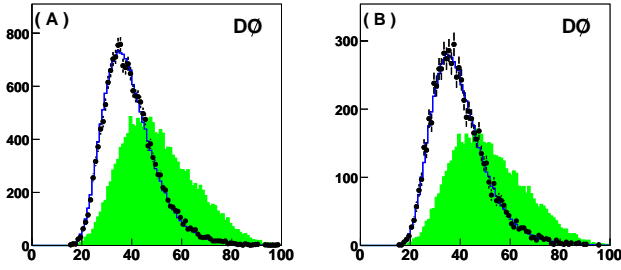


FIG. 6: The M_{min}^{34} distribution for single-tag events (A) and double-tag events (B). Shown are the data (points), the background (solid line) and the expected $t\bar{t}$ distribution (filled histogram) multiplied by 140(60) for the single(double)-tag analysis.

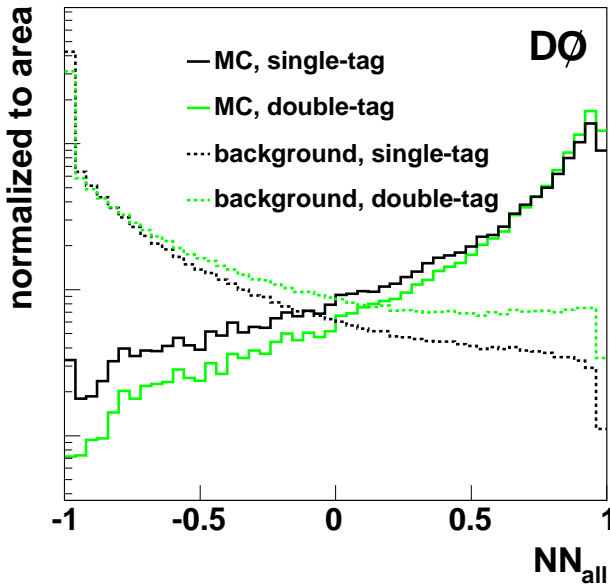


FIG. 7: The output discriminant of NN_{all} , an artificial neural network with six input nodes. NN_{all} is optimized to distinguish between fully hadronic $t\bar{t}$ Monte Carlo events (signal) and multijet production (background).

to-signal ratio in the untagged data allowed us to use untagged data as background input for the training of NN_{all} , while $t\bar{t}$ MC is used for the signal. Figure 7 shows the NN_{all} discriminant for $t\bar{t}$ signal and multijet background. Although the distributions for single- and double-tag events are different due to increased heavy flavor content in the double-tag sample, both samples show a clear discrimination between signal and background.

The overwhelming background also meant it was possible to use the entire (tagged and untagged) sample to estimate the background. For the loose and tight SVT, we derived a tag rate function (TRF) - the probability for a jet to have a secondary vertex tag - from the data with $N_{tags} \leq 1$. The TRF, $p_i = f_i(p_T)g_i(\phi)h_i(y)l_i(z_{PV})$ is parameterised in terms of the p_T , ϕ and y of the jet,

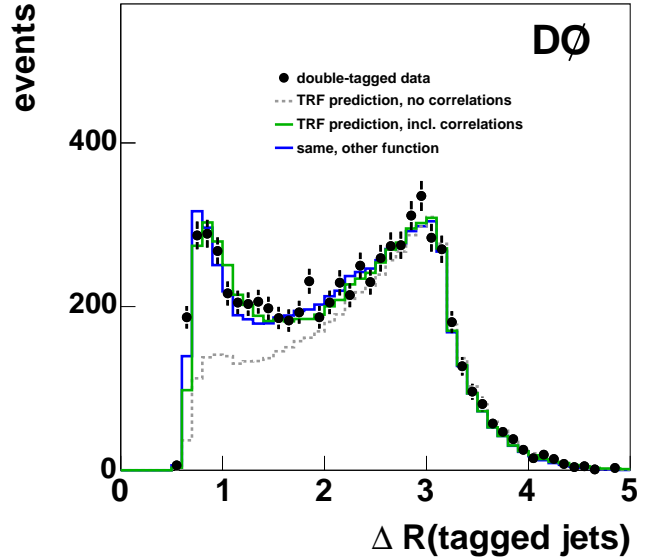
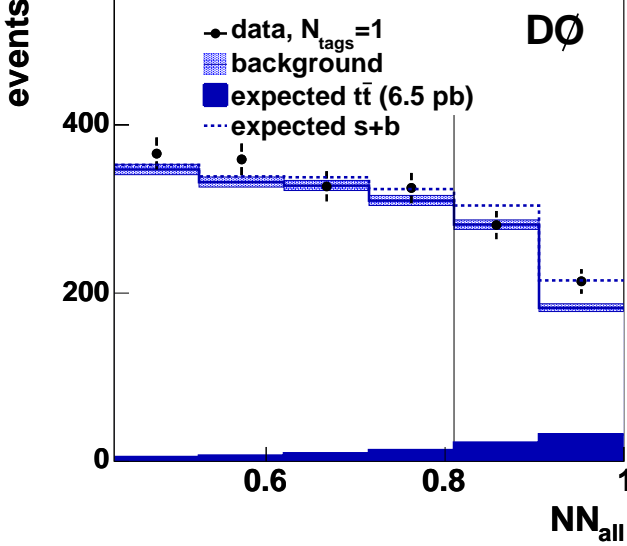


FIG. 8: The performance of the TRF prediction on double-tag events, with and without including the correlation factor C_{ij} , where two different functional parameterisations of C_{ij} are considered.

and the z -coordinate of the primary vertex of the event, z_{PV} , in four different H_T bins. To predict the number of tagged jets in the event, one has to presume there is no correlation between tagged jets, an assumption that is not true for double-tag events, where the probability to tag a second jet is greatly increased by the presence of $b\bar{b}$ +jets events in the sample. We correct for this with a correlation factor C_{ij} , that is parameterized as a function of the cone angle between the tagged jets, ΔR . Figure 8 shows the number of double-tagged events versus ΔR as observed in data, and the distribution as modeled by the TRF with and without including C_{ij} . We considered different parameterisations of C_{ij} and found that the choice of parameterisation had little effect on the shape of the modeled background distribution.

The probabilities p_i are used to assign a weight, the probability that the event could have a given number of tags, to every tagged and untagged event in the sample. To ensure the TRF prediction is accurate in the region of phase space outside the “background” peak of the neural network, we use the region $-0.7 < NN_{all} < 0.5$ to determine a normalization. In this region of phase space, $t\bar{t}$ content is negligible. A possible dependence on $t\bar{t}$ content was studied by the addition and/or subtraction of simulated $t\bar{t}$ events. Outside the background peak, the TRF predictions are corrected by: $SF_{TRF}^1 = 1.000 \pm 0.009$ for the single-tag analysis, and $SF_{TRF}^2 = 0.969 \pm 0.014$ for the double-tag analysis. The errors on the normalisation are taken into account as a systematic uncertainty on the number of background events.

Both analyses are expected to be dominated by back-

FIG. 9: NN_{all} output for single-tag events.

ground, even at large values of NN_{all} . Figures 9 and 10 show the distribution for data (points), the Monte Carlo simulation prediction equivalent to $\sigma_{t\bar{t}} = 6.5$ pb (filled histogram), the background prediction (line histogram) and the signal+background distribution (dashed histogram).

The cross section is calculated from the number of $t\bar{t}$ and background candidates above a value of the NN_{all} discriminant. The cut value is tuned to maximize the expected statistical significance - $s/\sqrt{s+b}$, where s and b are the number of expected signal and background events - of a cross section measurement, using the background distribution and simulated $t\bar{t}$ events as input[16]. For both analyses, the optimal expected statistical significance was on the order of 2 Gaussian standard deviations. The optimal cut for the single(double)-tag analysis was $NN_{all} \geq 0.81(0.78)$. Table II gives the observed numbers of events (N_{tags}^i), the background prediction (N_{bg}^i) and the efficiency for signal ($\varepsilon_{t\bar{t}}^i$) that can be used to calculate the $t\bar{t}$ production cross section via:

$$\sigma_{t\bar{t}} = \frac{N_{tags}^i - N_{bg}^i}{\varepsilon_{t\bar{t}}^i \mathcal{L}(1 - \varepsilon_{TRF}^i)}, \quad (2)$$

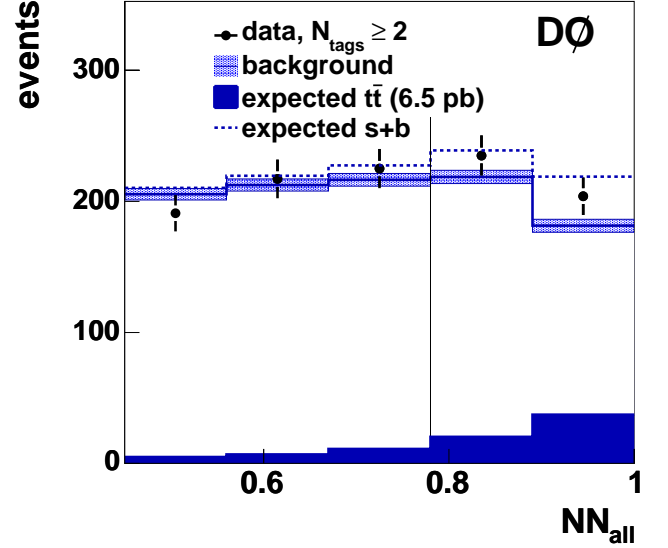
where i is 1 for the single-tag analysis and 2 for the double-tag analysis. The expected $t\bar{t}$ contamination of the background sample is corrected by a factor ε_{TRF}^i .

Table II lists the systematic uncertainties on the estimate of the number of background events, the selection efficiency and the background contamination. The first is uncorrelated between the two analyses, while the latter two are correlated as they were derived from the same Monte Carlo samples.

For the single-tag analysis, the systematic uncertainty on the selection efficiency is dominated by the uncer-

TABLE II: Overview of observed events, background predictions and efficiencies.

	symbol	analysis	value
observed events	N_{obs}^1	$N_{tags} = 1$	495
background events	N_{bg}^1	$N_{tags} = 1$	$464.3 \pm 4.6(\text{syst})$
$t\bar{t}$ efficiency	$\varepsilon_{t\bar{t}}^1$	$N_{tags} = 1$	$0.0242^{+0.0049}_{-0.0058}(\text{syst})$
$t\bar{t}$ contamination	ε_{TRF}^1	$N_{tags} = 1$	$0.245 \pm 0.031(\text{syst})$
observed events	N_{obs}^2	$N_{tags} \geq 2$	439
background events	N_{bg}^2	$N_{tags} \geq 2$	$400.2^{+7.3}_{-6.2}(\text{syst})$
$t\bar{t}$ efficiency	$\varepsilon_{t\bar{t}}^2$	$N_{tags} \geq 2$	$0.0254^{+0.0065}_{-0.0070}(\text{syst})$
$t\bar{t}$ contamination	ε_{TRF}^2	$N_{tags} \geq 2$	$0.194 \pm 0.048(\text{syst})$

FIG. 10: NN_{all} output for double-tag events.

tainty in the jet energy scale and identification. The uncertainty on the background prediction is dominated by the uncertainty of the TRF method and the uncertainty on ε_{TRF} is due to limited Monte Carlo statistics. For the double-tag analysis, the contribution from the uncertainty of the b quark jet identification becomes large enough to be an additional dominant systematic uncertainty on $\varepsilon_{t\bar{t}}$.

The single-tag analysis yields a cross section of $\sigma_{t\bar{t}} = 4.8^{+3.5}_{-3.5}(\text{stat})^{+1.5}_{-1.1}(\text{syst}) \pm 0.3(\text{lumi})$ pb, where the systematic uncertainty due to the integrated luminosity measurement is traditionally listed separately. For the double-tag analysis the value is $\sigma_{t\bar{t}} = 5.4^{+3.0}_{-2.9}(\text{stat})^{+2.0}_{-1.6}(\text{syst}) \pm 0.3(\text{lumi})$ pb. As the single-tag and double-tag analysis are measured on independent samples, the statistical uncertainties are uncorrelated. The uncertainties on the analysis efficiency are completely correlated. Taking all errors into account, a combined cross section measurement of $\sigma_{t\bar{t}} = 5.2^{+2.3}_{-2.2}(\text{stat})^{+1.6}_{-1.2}(\text{syst}) \pm 0.3(\text{lumi})$ pb is obtained, for a top mass of $m_t = 175 \text{ GeV}/c^2$. For a top mass

of $m_t = 165 \text{ GeV}/c^2$, the cross section is $\sigma_{t\bar{t}}(165) = 7.2^{+3.2}_{-3.1}(\text{stat})^{+2.3}_{-1.7}(\text{syst}) \pm 0.5(\text{lumi}) \text{ pb}$, while for a top mass of $m_t = 185 \text{ GeV}/c^2$ the value shifts down to $\sigma_{t\bar{t}}(185) = 5.0^{+2.2}_{-2.1}(\text{stat})^{+1.6}_{-1.2}(\text{syst}) \pm 0.3(\text{lumi}) \text{ pb}$.

In summary, we have measured the $t\bar{t}$ production cross section in $p\bar{p}$ interactions at $\sqrt{s} = 1.96 \text{ TeV}$ in the fully hadronic decay channel. We use lifetime b -tagging and an artificial neural network to distinguish $t\bar{t}$ from background. Our measurement yields $\sigma_{t\bar{t}} = 5.2^{+2.3}_{-2.2}(\text{stat})^{+1.6}_{-1.2}(\text{syst}) \pm 0.3(\text{lumi}) \text{ pb}$, in agreement with SM predictions and previous measurements.

We thank the staffs at Fermilab and collaborating in-

stitutions, and acknowledge support from the DOE and NSF (USA); CEA and CNRS/IN2P3 (France); FASI, Rosatom and RFBR (Russia); CAPES, CNPq, FAPERJ, FAPESP and FUNDUNESP (Brazil); DAE and DST (India); Colciencias (Colombia); CONACyT (Mexico); KRF and KOSEF (Korea); CONICET and UBACyT (Argentina); FOM (The Netherlands); PPARC (United Kingdom); MSMT (Czech Republic); CRC Program, CFI, NSERC and WestGrid Project (Canada); BMBF and DFG (Germany); SFI (Ireland); Research Corporation, Alexander von Humboldt Foundation, and the Marie Curie Program.

[*] Visitor from Purdue University Calumet, Hammond, Indiana, USA.

[†] Visitor from Helsinki Institute of Physics, Helsinki, Finland.

[1] DØ Collaboration, V. Abazov *et al.*, Phys. Rev. Lett. **94**, 221802 (2005).

[2] DØ Collaboration, V.M. Abazov *et al.*, arXiv:physics/0507191.

[3] DØ luminosity reference: T. Edwards *et al.*, FERMILAB-TM-2278-E (2004).

[4] G.C. Blazey *et al.*, U. Baur, R.K. Ellis and D. Zeppenfeld (ed.), Fermilab, Batavia, IL (2000).

[5] DØ Collaboration, B. Abazov *et al.*, to appear in Phys. Lett B (April 2005).

[6] DØ Collaboration, B. Abbott *et al.*, Phys. Rev. Lett. **83** 1908 (1999).

[7] R. Brun and F. Rademakers, Nucl. Inst. Meth. in Phys. Res. A **389** (1997) 81-86. See also <http://root.cern.ch/>.

[8] S. Eidelman *et al.*, Phys. Lett. B **592**, 1 (2004).

[9] GEANT reference: R. Brun and F. Carminati, CERN Program Library Long Writeup W5013, 1993 (unpublished).

[10] M.L. Mangano *et al.*, J. High Energy Phys. **07**, 001 (2003).

[11] T. Sjöstrand *et al.*, Comput. Phys. Commun. **135**, 238 (2001).

[12] D. Lange, Nucl. Instrum. Methods Phys. Res. A **462**, 152 (2001).

[13] J. Pumplin *et al.*, J. High Energy Phys. **0207**, 012 (2002) and D. Stump *et al.*, J. High Energy Phys. **0310**, 046 (2003).

[14] Rapidity y and pseudorapidity η are defined as functions of the polar angle θ and parameter β as $y(\theta, \beta) = \frac{1}{2} \ln[(1 + \beta \cos \theta)/(1 - \beta \cos \theta)]$ and $\eta(\theta) = y(\theta, 1)$, where β is the ratio of the particle's momentum to its energy.

[15] In principle, in the measurement presented in this letter, a correction to ensure a identical calorimeter response for jets in Monte Carlo simulation and data would be sufficient. The correction to particle level was chosen to remain consistent with DØ analyses in other $t\bar{t}$ production channels.

[16] The expected $t\bar{t}$ content used to tune the NN_{all} cut optimization is equivalent with a hypothetical cross section of $\sigma_{t\bar{t}} = 6.5 \text{ pb}$.